Investigation of Fluid-dynamics and Mass-transfer in a bubbly mixing layer by Euler-Euler simulation

Kappelt, C.; Rzehak, R.;

Originally published:

September 2022

Chemical Engineering Science 264(2022), 118147

DOI: https://doi.org/10.1016/j.ces.2022.118147

Perma-Link to Publication Repository of HZDR:

https://www.hzdr.de/publications/Publ-35557

Investigation of Fluid-dynamics and Mass-transfer in a Bubbly Mixing Layer by Euler-Euler Simulation

Carolin Kappelt, Roland Rzehak*

Helmholtz-Zentrum Dresden – Rossendorf, Institute of Fluid Dynamics,
Bautzner Landstrasse 400, D-01328 Dresden, Germany

Abstract

Mass transfer in bubbly flows is a field of obvious technological importance. On industrially relevant scales it may be studied by simulations based on the Euler-Euler two-fluid model, which however requires closure models for the interfacial exchange processes. Despite recently increased efforts, modelling of the exchange of mass between the phases is still much less developed than the corresponding exchange of momentum. The present study compares several proposed models for the mass transfer coefficient using a previously established set of closure relations for the purely fluid dynamical part of the problem. A set of experimental data for the absorption of O_2 into water in a bubbly mixing layer from the literature is used to assess their relative merits. A model for the pertinent material properties of this system has been assembled from available measurements. A rather sensitive dependence of the amount of absorbed O_2 is found on the pressure, which varies with the hydrostatic head above the test section.

Keywords: mass-transfer, dispersed gas-liquid multiphase flow, Euler-Euler two-fluid model, closure relations, CFD simulation, model validation

* Corresponding author. E-mail: r.rzehak@hzdr.de

1 INTRODUCTION

Mass-transfer between gas bubbles and the liquid surrounding them is an important phenomenon in chemical engineering and biotechnology as well as cleaning and purification processes in diverse fields of application. In comparison to merely fluid dynamical problems, the modeling of mass transfer phenomena in bubbly flows is developed much less. On the scale of technical equipment, simulations are feasible by means of the Eulerian framework of multiphase flow. For practical application this requires a closure relation for the mass transfer coefficient, the suitability of which has to be validated by comparing the simulations results to experimental data.

A review of earlier work in this field has been given in Rzehak and Krepper (2016) for purely physical mass transfer and in Krauß and Rzehak (2018, 2017) for the case with an accompanying chemical reaction. The topic has received continued high interest since then, especially with a focus on reactive systems such as CO_2 in aqueous NaOH (Hori et al. 2020) or NO in aqueous Fe^{II} complexes (Hlawitschka et al. 2017a), comprising both experiments (Kipping et al. 2020, Kovats et al. 2018) and simulations by the Euler-Euler and Euler-Lagrange methods (Taborda and Sommerfeld 2021, Hlawitschka et al. 2017b). Despite these recent advances, the quest for a well-validated and broadly applicable model for the bubbles' mass transfer coefficient remains an ongoing venture (Solsvik 2018).

For data serving the purpose of model validation it is essential that the concentration, phase fraction, and velocity fields are available with a decent resolution over the flow domain. In addition, measurements of the bubble size are required as well, since this quantity appears in virtually all of the closure models used in Euler-Euler simulations. Furthermore, it would be highly desirable that the data also contain some variation of this parameter so that a meaningful comparison between different models can be made. Sources of such data for cases involving mass transfer are much scarcer than for purely fluid dynamical problems. For the present investigation, the work of Ayed et al. (2007) is considered.

The fluid dynamic modeling used in the present work employs a baseline model established in Rzehak and Krepper (2013) and thoroughly validated in a number of studies since then for simple bubbly pipe flows and bubble columns (e.g. Rzehak et al. 2017, 2017a, 2015, Fleck and Rzehak 2019, Rzehak and Kriebitzsch 2015, Rzehak and Krepper 2015, 2013a, Ziegenhein et al. 2017, 2015, 2013), but also for more complex applications such as an airlift-column (Liao et al. 2016), a helical static mixer (Zidouni et al. 2015) and a stirred tank (Shi and Rzehak 2018). Since this model was shown to give consistently good agreement with experimental data over a significant range of conditions, it provides a reliable basis to describe the fluid dynamics of bubbly flows. For the present investigation, two correlations for the drag force are compared corresponding to different water quality. The general description of mass transfer follows Rzehak and Krepper (2016). For the mass transfer coefficient several correlations applied in previous works are evaluated. In the experiments of (Ayed et al. 2007) the transferred species was oxygen, O_2, and a model for the pertinent material properties is assembled from literature sources.

Detailed local information is available in the work of Ayed et al. (2007) in the form of lateral profiles taken at several axial locations, but only a single test condition has been considered. In addition to the concentration of dissolved O_2 in the liquid phase, also fluid dynamical observables have been measured. This provides in addition to the investigation of mass transfer models also a further qualification of the fluid dynamical part of the model for a configuration that is more complex than simple pipe flows or bubble columns.

In addition to the experiments, also Euler-Euler simulations have been presented by Ayed et al. (2007). As will be discussed, the closure models used for the fluid dynamical part are comparable to the present ones. However, upon careful inspection the source of the assumed correlation for the mass transfer coefficient and its applicability to the present case is unclear. Moreover, it is found that pressure has a significant effect on the amount of absorbed O_2. This makes the actual water level in the reservoir at the top of the column an important variable, which highlights the importance of complete specifications for test cases to be used in model validation.

The paper is organized as follows: A summary of the experiments is given in section 2. The applied models are described in section 3. Emphasis is put on the mass transfer part in section 3.1. For the fluid dynamical part a brief summary and a guide to previous work is given in section 3.2. The material model is furnished in section 3.3. In section 4, the simulation results are presented and comparison is made to the measurements. Finally, discussion is offered in section 5.

2 SUMMARY OF EXPERIMENTAL DATA

Ayed et al. (2007) considered bubbly flow in a mixing layer as sketched in Figure 1. The test section was a vertically oriented rectangular flow channel. The inlet at the bottom was composed of two square regions separated by a splitter plate. Inlet 1 was supplied with pure liquid while at inlet 2 a sparger consisting of 576 needles distributed evenly over the inlet area injected gas into the flowing liquid. The set values of liquid volume flux and gas fraction are summarized in Table 1. Materials used were pure oxygen (O_2) for the gas and water for the liquid. A small amount of oxygen corresponding to a mass fraction of $Y_L^{O_2}$ = 9.96e-6 was initially dissolved in the water. No statement concerning the water quality (clean or contaminated) is available. Temperature and pressure were at ambient values. However closer inspection of the setup revealed that there is a 0.6 m deep reservoir on top of the test section which is filled to an unknown level (Roig and Larue de Tournemine 2007, Figure 2). This leaves some uncertainty at which height precisely the system is actually open to the atmosphere.

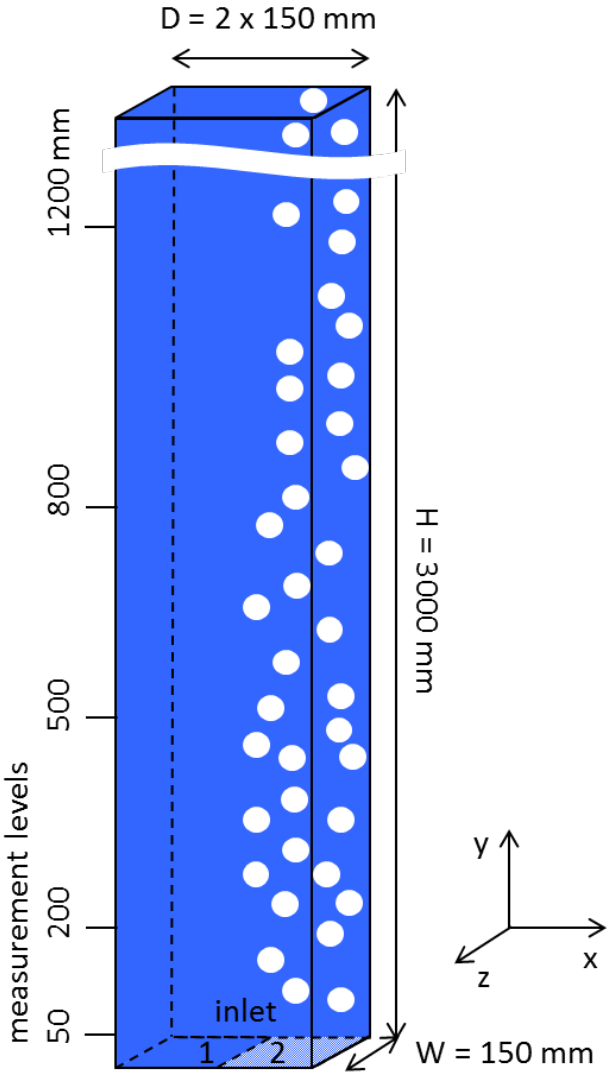

Figure 1: Sketch of the geometry for the test from Ayed et al. (2007).

test case	$J_L(in1)$	$J_L(in2)$	$\alpha_G(in1)$	$\alpha_G(in2)$	$Y_L^{O_2}(in1)$	$Y_L^{O_2}(in2)$	$\langle d_B \rangle$
Ayed et al. (2007)	m/s	m/s	%	%	-	-	mm
-	0.57	0.29	0.0	2.0	9.96e-6	9.96e-6	1.8

Table 1: Summary of parameters for the test of Ayed et al. (2007).

Measurements were taken along lateral profiles in the mid-plane of the channel at five axial locations above the inlet as indicated in

Figure 1. Measured quantities were gas fraction, bubble size, mean axial liquid velocity, axial liquid velocity fluctuations, relative velocity between gas and liquid, and oxygen concentration in the liquid. Oxygen concentration was measured by a Clark electrode probe. For the observables pertaining to the gas phase a two-point optical-fiber probe was used, while the liquid phase velocity was determined by a hot-film probe. Concerning the bubble size only minor variation with height was found, which indicates that processes of bubble-coalescence and -breakup are at most of minor importance. Averaging over all levels gave an average value of d_B = 1.8 mm with a standard deviation of 0.3 mm.

3 DESCRIPTION OF PHYSICAL MODELS

The main focus here is on the mass transfer part of the model, which is covered in section 3.1. A concise summary of the fluid dynamical part of the model is given in section 3.2, because this part was chosen to exactly match a baseline model that was validated in a number of previous studies. Full details of this model have been given e.g. in Rzehak and Krepper (2013) or Rzehak et al. (2017). A material model for the system of O_2 and water is finally presented in section 3.3.

3.1 Mass Transfer

To describe mass transfer phenomena, equations for the concentration of the transferred species, which appears as a solute in both phases, are required. These are summarized as

$$\frac{\partial}{\partial t}(\alpha_G \rho_G Y_G^A) + \nabla \cdot (\alpha_G \rho_G \boldsymbol{u}_G Y_G^A) = \nabla \cdot \left(\alpha_G \rho_G D_G^{eff,A} \nabla Y_G^A\right) + \Gamma_G^A \tag{1}$$

$$\frac{\partial}{\partial t}(\alpha_L \rho_L Y_L^A) + \nabla \cdot (\alpha_L \rho_L \boldsymbol{u}_L Y_L^A) = \nabla \cdot \left(\alpha_L \rho_L D_L^{eff,A} \nabla Y_L^A\right) + \Gamma_L^A \ . \tag{2}$$

Here, A denotes the transferred species, $Y^A = \rho^A/\rho$ is its mass fraction and $\rho = \sum_X \rho^X$ is the density of the multi-component mixture of which each phase consists. No separate equations are needed for the solute, since its mass fraction can be calculated from the constraint $\sum_X Y^X = 1$. Care should be taken not to confuse the mass concentration of a species in a mixture with the thermodynamic density of the pure substance although unfortunately the same letter ρ is conventionally used to denote both. The phase fraction α and phasic velocity $\boldsymbol{u}$ are obtained from the fluid dynamical part of the model (see section 3.2). The mass transfer sources for both phases are related as $\Gamma_G^A = -\Gamma_L^A$ to satisfy mass conservation and their sign is such that for absorption $\Gamma_L^A > 0$. Further models are needed for the effective diffusion coefficient $D^{eff,A}$ and the source terms due to transport across the phase interface Γ^A, which are described in the following.

Mass transfer through an element of the interface between gas and liquid is driven by the difference between the concentration Y^{A*} right at the interface, where both phases are assumed to be in equilibrium, and the concentration Y^A in the bulk of each phase. Frequently, the difference is small in the gas phase resulting in the one-sided model sketched in Figure 2. The mass transfer coefficient k_L is defined as the constant of proportionality between the mass flux G_L^A into the liquid and this concentration difference within the liquid, i.e.

$$G_L^A = k_L \rho_L (Y_L^{A*} - Y_L^A) \ . \tag{3}$$

k_L depends on details of the mass transport from the interface through the liquid boundary layer to the bulk within the liquid phase, which generally may comprise diffusive and convective contributions as well as turbulence effects. For a bubble, the overall mas transfer coefficient is obtained by summing the contributions from each interface element to give the mass flux through the entire bubble surface. It thus becomes a function of the bubble shape and the flow around it, both of which are determined by the bubble size, its velocity relative to the liquid and material parameters. Among the latter, the diffusivity appears directly in the mass transport problem, while viscosity and surface tension come into play indirectly by affecting the flow field.

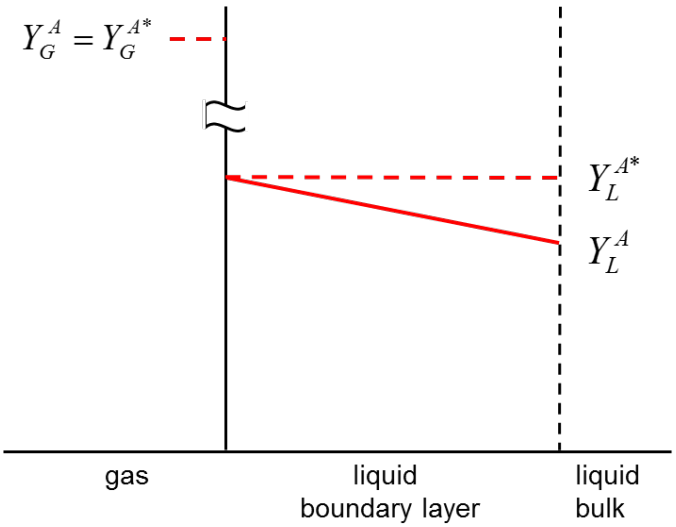

Figure 2: Simplified sketch of concentrations driving mass transfer across an interface.

The volumetric source term Γ_L^A is obtained from the mass flux G_L^A by multiplying with the interfacial area concentration a_I. Furthermore, concentrations in the gas and liquid at the interface are related by Henry's law with the constant denoted as He^A. Thus one obtains

$$\Gamma_L^A = k_L a_I \rho_L \left(He^A \, Y_G^A \frac{\rho_G}{\rho_L} - Y_L^A \right). \tag{4}$$

For the liquid side mass transfer coefficient k_L three correlations are considered which are expressed in terms of dimensionless variables, namely Sherwood number $Sh = k_L \, d_B / D_L^A$, Reynolds number $Re = |\boldsymbol{u}_G - \boldsymbol{u}_L| d_B \rho_L / \mu_L$, and Schmidt number $Sc = \mu_L / (\rho_L D_L^A)$. A comparison of all three correlations as function of Re is shown in the bottom part of Figure 3 below.

The first one,

$$Sh = \left(2 + \frac{0.651 \, (Re \, Sc)^{1.72}}{1 + (Re \, Sc)^{1.22}} \right) \left((1 + 0.433 \, Re^2)^{-1} + 4.23 \right)^{-0.055}, \tag{5}$$

was used in the simulations of Ayed et al. (2007) with reference to Mewes and Wiemann (2003), who in turn quote it as a result for spherical bubbles from Brauer (1981). This latter reference is obviously erroneous and should likely have been Brauer (1979) as also given by Ayed et al. (2007). Upon close inspection however, the expression for the last factor in Eq. (5) does not appear in Brauer (1979). Instead, a graphical result is displayed, from which a number of data points are shown in the top part of Figure 3 (crosses). As may be seen, these are very different from the expression given by Mewes and Wiemann (2003) (dotted line). Hence, the origin and meaning of Eq. (5) is somewhat unclear.

Therefore, a fit formula to the graphical result from Brauer (1979) was developed (solid line in the top part of in Figure 3) and is used in a second correlation for the mass transfer coefficient, namely

$$Sh = \left(2 + \frac{0.651 \, (Re \, Sc)^{1.72}}{1 + (Re \, Sc)^{1.22}} \right) \left(1 + \frac{0.037 \, Re^{0.9}}{1 + 0.05 \, Re^{0.9}} \right). \tag{6}$$

The results for spherical bubbles from Brauer (1979) on which Eq. (6) is is based were obtained by direct numerical simulations of the coupled equations for fluid dynamics and mass transfer. Surfactants were not included in the simulations, hence it corresponds to an absolutely clean bubble with a fully mobile interface. Conditions imposed at the bubble surface were a free slip condition for the fluid dynamical part and a fixed concentration for the mass transfer part. Accordingly, the internal circulation and the gas side resistance to mass transfer are neglected. Both of these assumptions are typically made for gas bubbles since the viscosity and diffusivity in the gas are much smaller than those in the liquid. The motion of the interface relative to the liquid is of course determined by the imposition of the spherical bubble shape, but within this assumption the development of the boundary layer from the stagnation point at the bubble front to detachment and wake formation and the rear end of the bubble are captured by the simulations.

Finally, a third correlation is considered that applies for deformed bubbles, i.e.

$$Sh = (2 + 0.015\, Re^{0.89} Sc^{0.7})\,. \qquad (7)$$

This also appeared in Brauer (1979) and was quoted by Mewes and Wiemann (2003). In addition it was compared with recent measurements on single bubbles (Merker et al. 2017) and applied in a number of other simulations including mass transfer (e.g. Krauß and Rzehak, 2018 and references therein). The correlation Eq. 7 was proposed by Brauer (1979) based on a review of experimental studies at varying Re and Sc. Unfortunately the water quality was not reported, so the interface mobility is not known with certainty. While the internal circulation and gas side resistance to mass transfer are included in principle, they are still small effects for the reasons mentioned above. The dominant effect distinguishing this model from the previous one is that the bubble shape and wobbling and their influence on the boundary layer development and wake formation are captured.

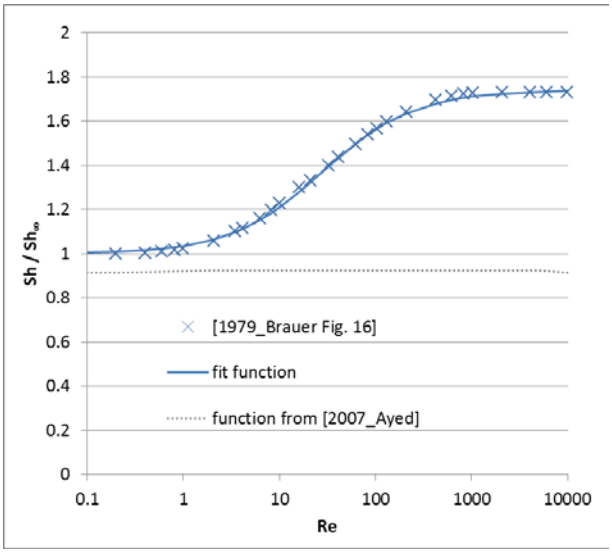

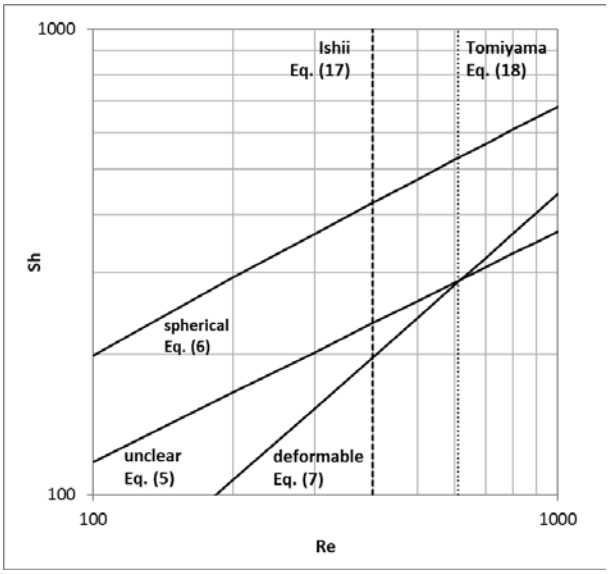

Figure 3: Comparison of mass transfer correlations. Top part: the last factor in the correlation from Mewes and Wiemann (2003), Eq. (5), (dotted line) is compared to the second factor in the correlation from Brauer (1979), Eq. (6), (crosses: scanned from the graphical result in the original work; solid line: fit formula used herein). Bottom part: the dependence of Sh on Re for $Sc = 371$ corresponding to O_2 in water at 25°C according to the correlations discussed in section 3.3 is compared for the correlations from Eqs. (5) to (7). Also indicated are the values of Re obtained for the terminal velocities for the two drag laws considered (see section 3.2).

The interfacial area concentration a_I in Eq. (4) is expressed as

$$a_I = \frac{6\alpha_G}{d_B} \tag{8}$$

by assuming spherical bubbles.

The Henry constant He^A, the molecular diffusion coefficient D_L^A, liquid density ρ_L and viscosity μ_L as well as the gas density ρ_G are obtained from the material model (see section 3.3) by inserting the appropriate values for the local temperature and pressure. The bubble size d_B is taken as a constant in accordance with the experiments as discussed in section 2.

The effective diffusion coefficients $D^{eff,A}$ consist of two contributions, a molecular one D^A and a turbulent one $D^{turb,A}$. The latter is typically dominant in the continuous liquid phase and calculated from the simple but frequently used assumption of unity Schmidt number (e.g. Cockx et al. 2001), i.e. from

$$Sc_L^{turb} = \frac{\nu_L^{turb}}{D_L^{turb,A}} = 1\,. \tag{9}$$

Herein, the turbulent kinematic viscosity ν_L^{turb} is obtained from the turbulence model (see section 3.2). No diffusive transport occurs between bubbles in the dispersed gas phase, i.e. $D_G^{eff\,A} = 0$.

245 Boundary conditions required to obtain a unique solution of Eqs. (1) and (2) are a specified
246 value of the mass fraction at an inlet, a vanishing normal derivative at an outlet, and $Y_G^A =$
247 $Y_L^A = 0$ on impermeable walls.

248

3.2 Fluid Dynamics

Fluid dynamic phenomena are described by balance equations for mass and momentum in each phase, which are summarized as follows. The continuity equations for both phases are

$$\frac{\partial}{\partial t}(\alpha_G \rho_G) + \nabla \cdot (\alpha_G \rho_G \boldsymbol{u}_G) = \Gamma_G^A \tag{10}$$

$$\frac{\partial}{\partial t}(\alpha_L \rho_L) + \nabla \cdot (\alpha_L \rho_L \boldsymbol{u}_L) = \Gamma_L^A \,, \tag{11}$$

and the momentum equations read

$$\frac{\partial}{\partial t}(\alpha_G \rho_G \boldsymbol{u}_G) + \nabla \cdot (\alpha_G \rho_G \boldsymbol{u}_G \otimes \boldsymbol{u}_G) = -\alpha_G \nabla p_G + \nabla \cdot (\alpha_G \mathbf{T}_G) + \alpha_G \rho_G \boldsymbol{g} + \boldsymbol{F}_G^{inter} + \boldsymbol{\Phi}_G^A \tag{12}$$

$$\frac{\partial}{\partial t}(\alpha_L \rho_L \boldsymbol{u}_L) + \nabla \cdot (\alpha_L \rho_L \boldsymbol{u}_L \otimes \boldsymbol{u}_L) = -\alpha_L \nabla p_L + \nabla \cdot (\alpha_L \mathbf{T}_L) + \alpha_L \rho_L \boldsymbol{g} + \boldsymbol{F}_L^{inter} + \boldsymbol{\Phi}_L^A \,. \tag{13}$$

Details on the derivation of these equations are available in several monographs (e.g. Drew and Passman 1998, Yeoh and Tu 2010, Ishii and Hibiki 2011).

The last terms on the right in in Eqs. (12) and (13) represent sources due to the mass transfer. The mass sources Γ^A are the same as already discussed in section 3.1. The so-called secondary momentum sources $\boldsymbol{\Phi}^A$ represent the momentum carried along by the transferred mass. A physical model for these sources consistent with all other aspects of the overall model is given by

$$\boldsymbol{\Phi}_G^A = -max(0, \Gamma_L^A)\, \boldsymbol{u}_G - min(0, \Gamma_L^A)\, \boldsymbol{u}_L \tag{14}$$

$$\boldsymbol{\Phi}_L^A = max(0, \Gamma_L^A)\, \boldsymbol{u}_G + min(0, \Gamma_L^A)\, \boldsymbol{u}_L \,. \tag{15}$$

Since for the present application only a small amount of mass is transferred between the phases, their magnitude is likewise small, but they are nonetheless included for the sake of completeness.

The stress tensor is given by

$$\mathbf{T} = \mu^{eff}(\nabla \boldsymbol{u} + (\nabla \boldsymbol{u})^T) \,, \tag{16}$$

where the effective dynamic viscosity μ^{eff} comprises a viscous and a turbulent contribution. For the liquid phase, the latter is calculated based on a k-ω SST model (Menter 2009). According to the baseline model applied here, source terms are added to the base model, which account for the bubble- induced turbulence (e.g. Rzehak and Krepper 2013a, Rzehak and Kriebitzsch 2015, Ziegenhein et al. 2017, Parekh and Rzehak 2018). For the gas phase, turbulence may be neglected because of the low gas density and the small spatial scales imposed by the bubble size, i.e. $\mu_G^{eff} = 0$.

The primary momentum sources $\boldsymbol{F}^{inter}$ represent the direct transfer of momentum across the interface and are related as $\boldsymbol{F}_G^{inter} = -\boldsymbol{F}_L^{inter}$ to satisfy momentum conservation. They comprise several different contributions and the closure relation used for each of these according to the applied baseline model is shown in Table 2 (e.g. Ziegenhein et al. 2013, Rzehak et al. 2015, Rzehak and Krepper 2015, or Rzehak et al. 2017a). The drag force

correlation of Ishii and Zuber (1979) used in the original baseline model corresponds to a contaminated water quality. In addition, a correlation proposed by Tomiyama et al. (1998) for clean water is considered. To be definite, the correlation of Ishii and Zuber (1979) reads

$$C_D = \max\left(\frac{24}{Re}(1 + 0.1\, Re^{0.75}), \min\left(\frac{2}{3}\sqrt{Eo}, \frac{8}{3}\right)\right), \tag{17}$$

while that of Tomiyama et al. (1998) is given by

$$C_D = \max\left(\min\left(\frac{16}{Re}(1 + 0.15\, Re^{0.687}), \frac{48}{Re}\right), \frac{8}{3}\frac{Eo}{Eo + 4}\right). \tag{18}$$

Two further relations are required to complete the above system of equations. With the assumption that each phase is incompressible, these are provided by conservation of volume, expressed as $\alpha_G + \alpha_L = 1$, and equilibrium of pressures, expressed as $p_G = p_L = p$.

Boundary conditions on solid walls are no-slip for the liquid and free slip for gas phase. The latter assumes that direct contacts between the bubbles and the walls can be neglected. The need to resolve the viscous boundary layer is avoided by applying a single phase turbulent wall function. At an inlet, profiles for the gas fraction and gas and liquid velocities are prescribed. Pressure is imposed as an outlet condition together with vanishing tangential velocity components and a vanishing normal derivative of gas fraction.

Table 2: Summary of bubble force correlations.

force	reference
drag (contaminated condition)	Ishii and Zuber (1979)
drag (clean condition)	Tomiyama et al. (1998)
shear lift	Tomiyama et al. (2002)
wall lift	Hosokawa et al. (2002)
turbulent dispersion	Burns et al. (2004)
virtual mass	constant coefficient C_{VM} = ½

3.3 Material Properties

The present section summarizes correlations assembled from the literature to model the temperature dependence of solubility and diffusivity of O_2 in water, surface tension between O_2 and water as well as viscosity and density of water and gaseous O_2. All correlations are valid at atmospheric pressure.

3.3.1 Solubility

The solubility of O_2 in water is quite well studied. A rather recent compilation of data and assessment of correlations for the Henry constant is given in Clever et al. (2014). In this review, the most precise measurements are attributed to Rettich et al. (2000). These are shown in Figure 4 together with a correlation based on the recommended one from Clever et al. (2014). Since the results of Clever et al. (2014) and Rettich et al. (2000) were expressed in units of 1/Pa rather than mol/mol as desired here, these results were multiplied by ρ^{H_2O} / M^{H_2O} where ρ^{H_2O} was determined in accordance with Rettich et al. (2000) from a correlation due to Kell (1975) and $M^{H_2O} = 0.018\, kg/mol$. Then the fit coefficients were adjusted to get the desired result in a single pass as

$$\mathrm{He} = R\,T \exp\left(-4.072752 - \frac{5756.888\,[K]}{T} + \frac{1075294\,[K^2]}{T^2}\right) \cdot \left[\frac{mol}{J}\right] . \qquad (19)$$

It may be noted that a three-parameter fit formula of different form proposed in the earlier review of Battino et al. (1983) yields numerically the same results. A simpler two-parameter fit due to Sander (2015) applies only to a more limited range around room temperature.

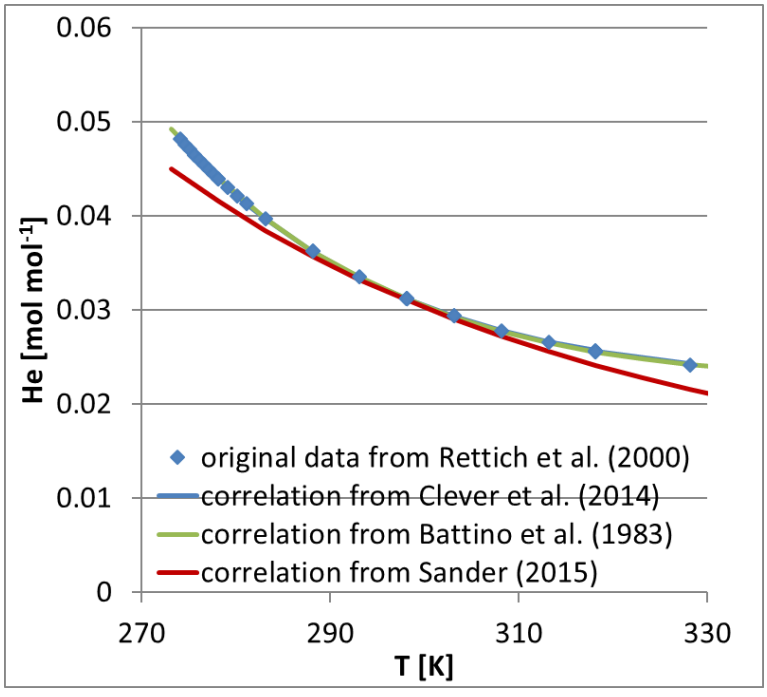

Figure 4: Henry constant for O_2 in water.

3.3.2 Diffusivity

As shown in Figure 5, data on the diffusivity of O_2 in water found in the literature (Akgerman and Gainer 1972, Verhallen et al. 1984, Han and Bartels 1996) exhibit a rather large spread in particular at elevated temperatures. Since a detailed assessment of the accuracy of the different measurements is not possible here, we have chosen the older but more frequently relied on data compiled by Akgerman and Gainer (1972) which comprise results from the earlier works of Himmelblau (1964), Ferrell and Himmelblau (1967), Wise and Houghton (1966) and a few smaller studies. These data are fitted by correlation

$$D_L^{O_2} = \exp\left(1.228 + \frac{2100\,[K]}{T} - \frac{657600\,[K12\,]}{T^2}\right) \cdot 10^{-9} \left[\frac{m^2}{s}\right]. \qquad (20)$$

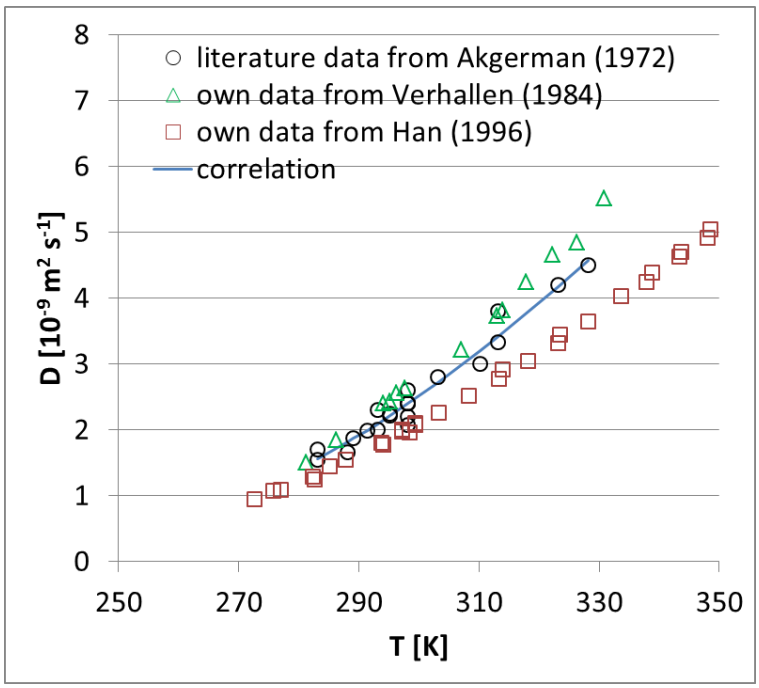

Figure 5: Diffusivity of O_2 in water.

3.3.3 Surface Tension

Data on the surface tension between mutually saturated mixtures of O_2 and water could not be found in the literature. However, for non-adsorbing gases the surface tension to the same liquid is typically the same. Therefore, we here substitute the surface tension for water with its own vapor which is quite well characterized (Vargaftik et al. 1983). From Figure 6, it is seen that these data are undistinguishable from data on air in contact with water (Gray, 1957, sect. 2p-2). In a range of temperatures around ambient conditions these data are well represented by a linear temperature dependence

$$\sigma = \left(122.37 - 0.1691\,\frac{T}{[K]}\right) \cdot 10^{-3} \left[\frac{N}{m}\right], \qquad (21)$$

which is also shown in Figure 6.

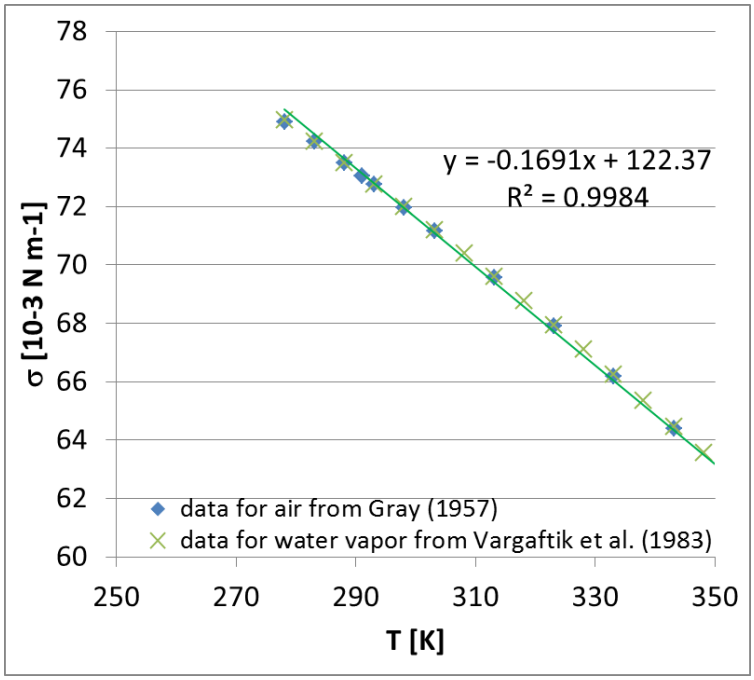

Figure 6: Surface tension of gases in water.

3.3.4 Viscosity

In the dilute limit, the presence of O_2 in the liquid phase may be neglected. For the viscosity of pure water a highly accurate description valid over a very large range of conditions is available (Huber et al. 2009) which is adopted by the IAPWS. However, sometimes a simpler correlation with a smaller range of applicability is advantageous to work with. To this end the Vogel-Fulcher-Tammann type formula

$$\mu_L^{H_2O} = \exp\left(3.184 + \frac{570.6[\mathrm{K}]}{\mathrm{T} - 140[\mathrm{K}]}\right) \cdot 10^{-6}[Pa\ s] \tag{22}$$

has been shown to provide a good description in the range from 5 … 95 °C (Rzehak and Krepper 2016).

For the gas phase Sutherland's formula is applied (e.g. Chapman and Cowling 1970, sect. 12.32), i.e.

$$\mu_G = \mu_{ref}\left(\frac{T}{T_{ref}}\right)^{3/2}\frac{T_{ref} + T_S}{T + T_S}, \tag{23}$$

where μ_{ref} is the viscosity at the reference temperature T_{ref} and T_S is a material dependent constant. The parameters for O_2 and air are summarized in Table 3.

gas	$T_S\ [K]$	$T_0\ [K]$	$\mu_0\ [10^{-6} Pa\ s]$
O_2	127	292.25	20.18

Table 3: Parameters for Sutherland correlation Eq. (23).

3.3.5 Density

Similarly, for the density of pure water the most accurate and complete description adopted by the IAPWS is given in Wagner and Pruß (2002). A simpler and more easily applicable quadratic fit formula

$$\rho_L^{H_2O} = \left(-0.0035\left(\frac{\mathrm{T}}{[\mathrm{K}]}\right)^2 + 1.824\frac{\mathrm{T}}{[\mathrm{K}]} + 763.42\right)\cdot\left[\frac{kg}{m^3}\right], \tag{24}$$

can be applied in the range from 5 … 95 °C (Rzehak and Krepper 2016).

The gas phase is modeled as an ideal gas or an ideal mixture thereof, i.e. the gas density given by

$$\rho_G = \frac{p\,M_G}{R\,T}, \tag{25}$$

where $\boldsymbol{M^{O_2} = 32.0\ \mathrm{kg}/\mathrm{kmol}}$ is the molar mass of O_2 and $\boldsymbol{R}$ is the universal gas constant. The pressure in Eq. (25) is the local fluid pressure, which varies over the height of the fluid domain mainly due to hydrostatics. As it will turn out this variation has a significant influence on the equilibrium at the interface. In principle a Laplace pressure of $\boldsymbol{4\,\sigma/d_B}$ should also be included, but this term is negligibly small for the present applications.

4 SIMULATION RESULTS

To perform the simulations the commercial software ANSYS CFX 17.2 is used. Due to a lack of symmetry in the geometry and boundary conditions, a fully three-dimensional simulation is run. A grid spacing of 5 mm in the lateral directions and stretched by a factor of 6 in the axial direction was determined to provide a reasonably well converged solution in a grid independency study. Concentrations, phase fractions, and phasic velocities at the two inlets are set according to the experimental description given in Section 2. For the turbulence, generic values of intensity (5%) and viscosity ratio (10) are imposed. Uniform distributions of all of these quantities over each inlet are assumed. Pressure at the outlet is set to atmospheric pressure unless stated otherwise. This corresponds to neglecting the hydrostatic head of the water in the reservoir above the test section. Based on the measurements dicussed in Section 2, the bubble size distribution may be taken as monodisperse with a constant bubble size. The experimentally determined mean value of d_B = 1.8 mm is used. Material properties according to the correlations of section 3.3 are evaluated at a temperature of 25 °C and the local pressure. In the course of the investigation, several model variants are considered, which are summarized in Table 4 for convenience. More detailed explanations are provided in the text.

designation	drag force model	mass transfer coefficient model	pressure
ShConst-CdTomi	Eq. (18)	$Sh = 400$	reservoir empty
ShConst-CdIshii	Eq. (17)	$Sh = 330$	reservoir empty
ShZero-CdTomi	Eq. (18)	$Sh = 0$	reservoir empty
ShZero-CdIshii	Eq. (17)	$Sh = 0$	reservoir empty
ShDef-CdTomi	Eq. (18)	Eq. (7)	reservoir empty
ShSph-CdIshii	Eq. (17)	Eq. (5)	reservoir empty
ShXxx-CdIshii	Eq. (17)	Eq. (6)	reservoir empty
ShDef-CdTomi-pressure	Eq. (18)	Eq. (7)	reservoir full
ShXxx-CdIshii-pressure	Eq. (17)	Eq. (6)	reservoir full

Table 4: Summary of investigated model variants.

4.1 Fluid Dynamics

Turning first to the fluid dynamics, results from experiment (symbols) and simulations (lines) are displayed in Figure 7 and Figure 8. Lateral profiles of gas fraction, liquid velocity and turbulent kinetic energy, as well as relative velocity between liquid and gas are shown at different locations along the test section. Since in the experiments only liquid velocity fluctuations in the axial direction have been recorded, isotropy is assumed like in Ayed et al. (2007) to express the turbulent kinetic energy as $\kappa_L = 3u_L'^2/2$. In the simulations, the two models for the drag force described in section 3.2 are compared, one being valid for contaminated interfaces (thick lines, labeled “Ishii”) while the other one was proposed for clean interfaces (thin lines, labeled “Tomi”). Each of these models is combined with two prescriptions for the mass transfer, which has either been negelcted (solid lines labeled

"ShZero") or set to an adjusted value as described further below in section 4.2 (dotted lines labeled "ShConst").

From the comparison of the two mass transfer prescriptions it is seen that for the present case, where the bubble size remains unaffected and the only action of the mass transfer on the fluid dynamics comes from the secondary momentum sources in Eqs. (14) and (15), there is only a minor effect. This influence of the mass transfer is most visible in the gas fractions at the highest level, but even there it is much smaller than that of the different drag forces. Otherwise, the effect is sometimes hardly discerned at all. Hence, this may be termed a one-way-coupling situation, in which the fluid dynamics of course affects the mass transfer, but not vice versa.

Looking in more detail at the flow development, it can be seen in qualitative terms that the liquid velocities on both sides, left without and right with gas injection, tend to equalize up to a height of around 500 mm. This would be expected also for a single phase flow due to the action of viscosity. In the present multiphase flow, the liquid on the right with gas injection is further accelerated due to momentum transfer from the buoyant gas. Therefore, from around 800 mm height on, the liquid velocity on the right exceeds that on the left side. Near the inlet, the gas content is distributed almost uniformly over the cross section of the right side of the channel, where the injection takes place. The left side of the channel remains free of gas over the entire height where measurements are taken. In fact, with increasing height the gas is continually shifted away from the channel center and towards the right wall. This can be attributed to the action of the lift force. The level of turbulence is significantly higher on the right side of the channel (where gas is injected) than on the left side of the channel (without gas injection) at all height levels. This is a clear signature of the bubble-induced turbulence. At the lower heights a peak in the turbulent kinetic energy is seen at the position of the splitter plate separating the two inlet regions which is caused by the strong shear gradient at this position. Also caused by shear turbulence is the peak developing with increasing height near the left wall of the channel where no gas is present.

Quantitatively, differences between the two drag models are most pronounced for the relative velocity between gas and liquid phase shown in Figure 8, hence these are discussed first. As is well known, the rise velocity is higher for clean bubbles than for contaminated ones which is also seen in the simulations. In comparison with the experimental data (symbols), the measurements are closer to the calculations for the clean case (thin lines) at the lowest level and closer to the calculations for the contaminated case (thick lines) at the highest level. This suggests the possibility that the bubbles are clean when they are injected in the system but collect contaminations during their rise. Taking into account the intermediate levels, this picture is not so clear anymore, hence it must be left as a hypothesis. It can be stated clearly however, that the calculations for clean and contaminated cases provide upper and lower bounds for the observed behavior.

Results for gas fraction, liquid velocity, and turbulent kinetic energy are collected in Figure 7. Smaller differences between the simulations based on the two drag models are seen which can be understood as consequences of the different relative velocities. A higher relative velocity of the bubbles tends to decrease the residence time of the bubbles which leads to a lower observed gas content. Hence, gas fractions calculated for the clean case (thin lines) tend

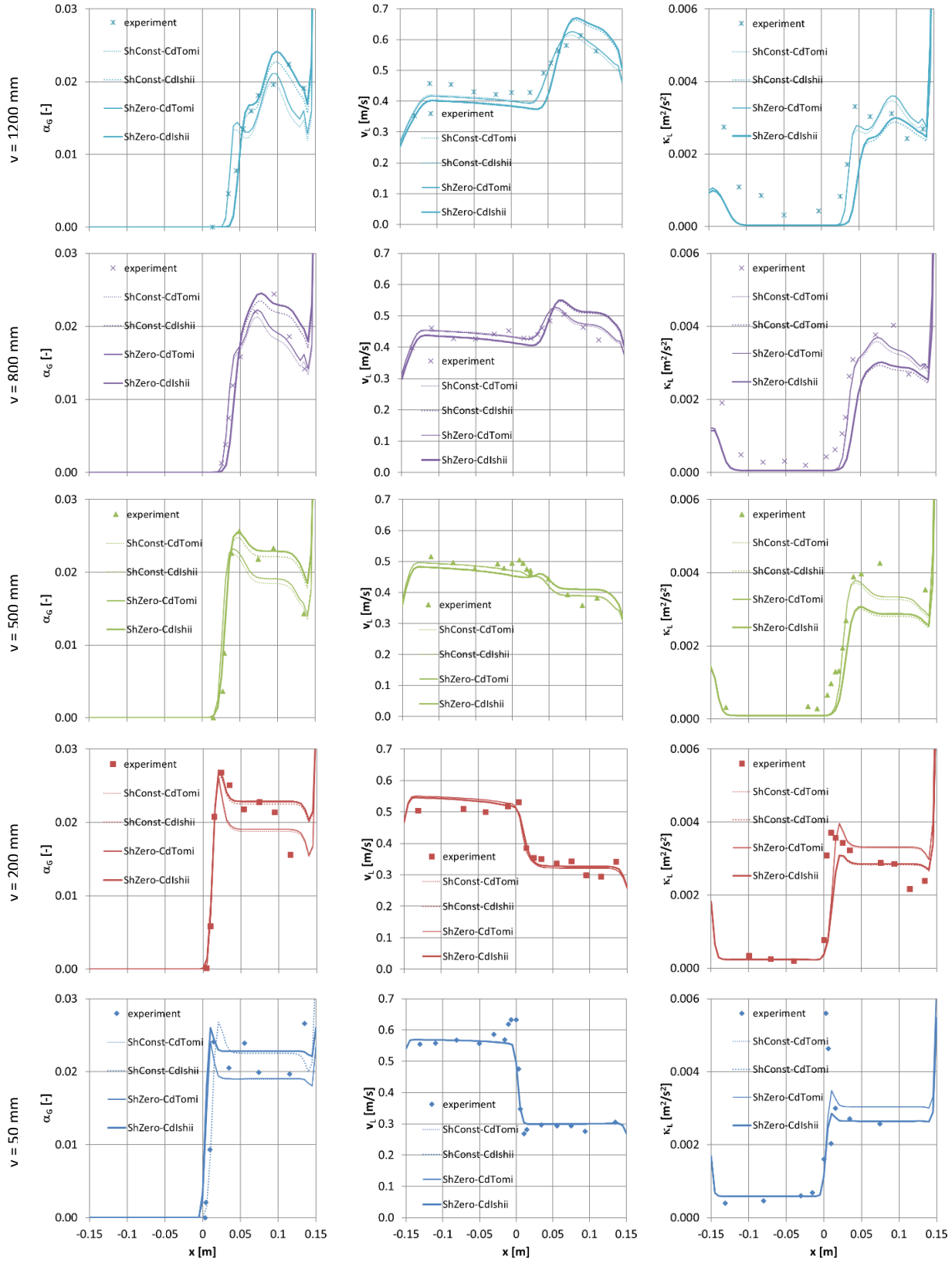

Figure 7: Comparison of experimental data (symbols) and simulation results (lines) using several models as described in the text. Lateral profiles are shown at different locations in the test section as indicated on the left of each row for gas fraction α_G (left column), liquid velocity v_L (middle column), and turbulent kinetic energy κ_L (right column).

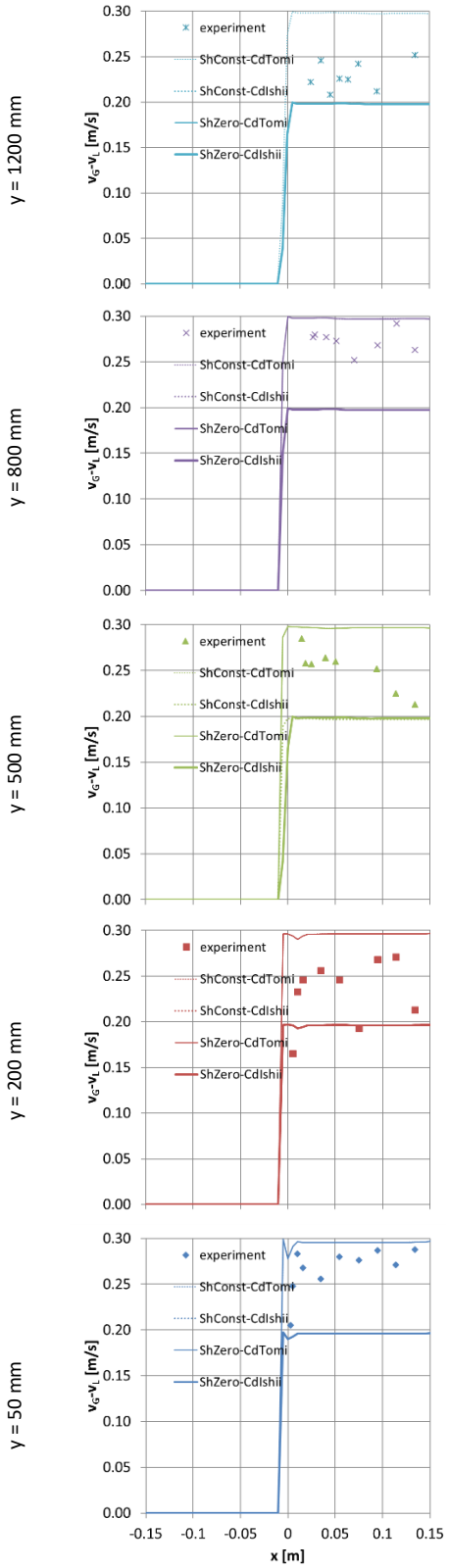

444 Figure 8: Comparison of experimental data (symbols) and simulation results (lines) using
445 several models as described in the text. Lateral profiles are shown at different locations along
446 the test section as indicated on the left of each row for the relative velocity $v_G - v_L$.

447

to be lower than those calculated for the contaminated case (thick lines). Due to the higher gas content, a larger amount of momentum is transferrred from the gas to the liquid phase which gives a higher liquid velocity in the right part of the test sction where gas is present for the contaminated case than for the clean case. Likewise a higher turbulent kinetic energy might be expected since the contribution to the bubble-induced turbulence is proportional to the gas fraction. However, it is also proportional to the relative velocity which is higher for the clean than for the contaminated case. Of the two competing effects the latter is seen to dominate.

Overall agreement between simulation results (lines) and and experimental data (symbols) is quite good for both drag force models. The model of Ishii and Zuber (1979) for contaminated interfaces comes a bit closer to the measurements for the gas fraction while the model of Tomiyama et al. (1998) for clean interfaces matches the liquid velocity and turbulent kinetic energy a bit better. The peak in turbulent kinetic energy seen in the experiment for the lowest height levels at the location of the splitter plate is significantly underestimated in the simulations. The same holds for the peak near the left channel wall that becomes most prominent at the highest levels. Both of these are likely due to shortcomings of the shear-induced turbulence modeling by the k-ω SST model. In addition, the simulations show pronounced peaks in gas fraction and turbulent kinetic energy near the right channel wall. Since these are below the spatial resolution of the measurements, their significance remains open.

4.2 Mass Transfer

Concerning mass transfer several different model variants are compared. In addition to the choice of the model for the mass transfer coeffcient (see Eqs. (5) to (7)) simulation results for the mass transfer also depend on the drag model, because this determines the bubble Reynolds-number. To keep the number of different variants tractable, the Ishii-Zuber drag model for contaminated bubbles is combined with the mass transfer coeffcient models of Eqs. (5) (designated as ShXxx-CdIshii) and (6) (designated as ShSph-CdIshii) for spherical bubbles, since the shape of contaminated bubbles is closer to spherical. For deformable clean bubbles the Tomiyama drag model is combined with the mass transfer coeffcient models of Eqs. (7) (designated as ShDef-CdTomi). A further significant dependence is found on the pressure, which in the experiment depends on the water level in the reservoir above the test section. This effect is caused by a corresponding change in the gas density according to the ideal gas law Eq. (25), which in turn appears in the mass transfer source Eq. (4). To assess this effect, in addition to the standard setting corresponding to an empty reservoir, also the case of a completely filled reservoir is considered (the latter identyfied by appending -pressure to the designation).

A comparison of the above variants is made for the concentration profiles of O_2 in the liquid at the highest level in the test section, where the differences are most pronounced. From the results shown in Figure 9, it may be seen that no model variant gives an entirely satisfactory match with the measurements. With the imposed concentration at the inlet as the reference, the spherical model (ShSph-CdIshii) overpredicts the measured concentrations by ~20% while the deformable model (ShDef-CdTomi) underpredicts them by a similar amount. The model of somewhat unclear origin (ShXxx-CdIshii), although decribed as applying to spherical bubbles by Mewes and Wiemann (2003) gives more similar results as the one for deformable

bubbles. Differences arising from the drag model appear small compared to differences arising from the mass transfer model. The effect of an increased pressure due the condition of a filled reservoir at the top of the test section (ShDef-CdTomi-pressure and ShXxx-CdIshii-pressure) is to increase the concentration cutting the difference to the measurement in half.

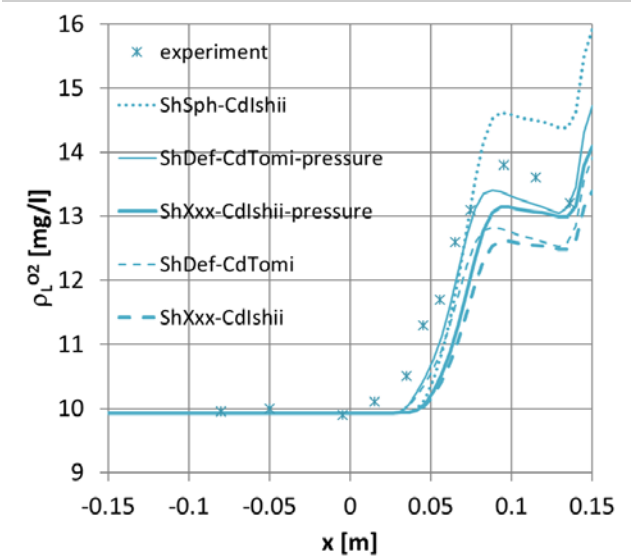

Figure 9: Comparison of experimental data (symbols) and simulation results (lines) using several models as described in the text. Lateral profiles are shown at highest level of the test section (y = 1200 mm) for the mass concentration of oxygen in the liquid $\rho_L^{O_2}$.

It is clear from the definitions in section 3.1 that the mass transfer coefficient does not vary throughout the flow domain. Thus, each mass transfer correlation only picks a constant value according to the overall flow parameters. In order to see how the development of the concentration profiles within the flow domain can be represented in the simulations, an adjusted value of the mass transfer coefficient has been determined that matches the data at the highest level (designated as ShConst). Values provding the best match are Sh = 330 for the Ishii-Zuber drag law and Sh = 400 for the Tomiyama drag law.

These results are shown in Figure 10. As may be expected, the concentration of oxygen in the liquid phase increases with increasing height. The shape of the concentration profiles follows the distribution of the gas fraction rather closely. In the left part of the channel, where no gas is injected, the concentration stays at its inlet value over the entire height where measurments are taken. With the adjustment at the highest level, the overall agreement between simulated (lines) and measured (symbols) concentrations of O_2 at the lower levels is quite good. Only at the lowest level (y = 50mm) the measured data are significantly underpredicted. Concerning the shape of the concentration profiles, the step between the two streams of the mxing layer is captured rather well. However, the dip at the nearest measurement point to the wall is not reproduced by the simulations. Still closer to the wall the simulations results show a steep increase similar as already observed for the gas fractions. Differences between the two drag models are found to be only small.

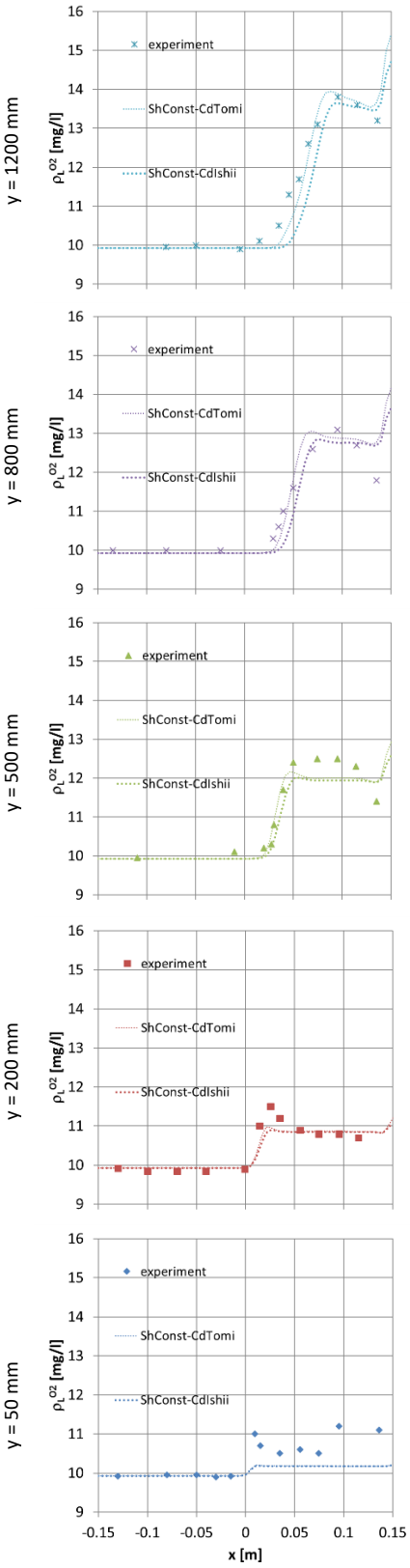

Figure 10: Comparison of experimental data (symbols) and simulation results (lines) using several models as described in the text. Lateral profiles are shown at different locations along the test section as indicated on the left of each row for the mass concentration of oxygen in the liquid $\rho_L^{O_2}$.

5 DISCUSSION AND CONCLUSIONS

Concerning fluid dynamics, quite good agreement was found for all of the measured quantities, namely gas fraction, mean liquid velocity, liquid turbulent kinetic energy, and relative velocity between the phases. The biggest uncertainty comes from the unknown water quality which has a significant impact on the relative velocity, that in turn affects all other fluid dynamic aspects as well as the mass transfer. In the present work, two different drag models from Ishii and Zuber (1979) and Tomiyama et al. (1998) corresponding to contaminated and clean conditions, respectively, were applied. Simulation results from these two models bracket the measured relative velocities and give approximate bounds for the other observables. Since water quality is difficult to control in practical applications this finding is quite useful. Comparison at different positions along the test section indicates the possibility that clean conditions prevail at the inlet but contaminations are accumulated on the gas-liquid interfaces during the flow. A more precise analysis is impeded by superimposed statistical variations in the measured data. However, to capture such effects the commonly used model frameworks would need to be substantially augmented by equations describing the contaminant concentration in the bulk and at the interfaces as well as models for the adsorption process.

Concerning mass transfer, none of the simple but frequently used correlations for the mass transfer coefficient of single bubbles that were compared gave an entirely satisfactory agreement with the measured concentrations. Assuming the most favorable condition for the pressure, the model for deformable bubbles from Brauer (1979) and the model of somewhat unclear origin used by Ayed et al. (2007) come within reach of the measurements. Which drag law is used in conjunction with the mass transfer model appears to be of minor importance. However, due to the uncertainties involved and the restriction of the test case to only a single value of the bubble size a definite recommendation for their general use cannot yet be given. Hence, to obtain a general correlation for the mass transfer coefficient of single bubbles that applies in a wide range of relevant parameters including different regimes of bubble shape and dynamics further investigations are necessary. A related aspect of the overall model that should be considered further is a more refined model describing the turbulent diffusivity depending on the local flow conditions by additional model equations for the variance of concentration fluctuations and its dissipation rate, as considered e.g. by Zhang et al. (2018), rather than just using a constant turbulent Schmidt number. A final minor issue in this context that nonetheless deserves to be improved is a lack of precise data on the diffusivity of O_2 in water.

Comparison may also be made with the previous simulation model by Ayed et al. (2007). The main difference concerning the applied closures is that these authors use a more elaborate turbulence model that treats shear- and bubble-induced turbulence as separate fields, while in the present work no such distinction is made and a single field representing the sum of both is used. While the model of Ayed et al. (2007) is potentially more general, it also requires further assumptions to be introduced in order to model the coupling between the fields relating to which hardly any evidence is available. As the present results show, at least for the conditions investigated no benefit results from the more complex model.

Comparing the simulation results mostly similar observations are made. In particular, the peak near the right channel wall in the gas fraction, turbulent kinetic energy, and oxygen concentration is also found in the simulations of Ayed et al. (2007) although for the concentration it is of lower magnitude there. Likewise, the underprediction of the peak in

turbulent kinetic energy near the left channel wall also occurs in the simulations of Ayed et al. (2007). However their simulations overpredict TKE peak at splitter plate for the second height level, which is likely related to the different inlet conditions, which they took from the measured profiles at the lowest lowest instead of constant generic values as used here. The biggest difference is that in the simulations of Ayed et al. (2007) the transition between the two streams occurs further towards the right channel wall for the turbulent kinetic energy as well as for the gas fraction and oxygen concentration. In this regard the present simulations are closer to the measured data. The difference can be traced to different profiles of turbulent viscosity and thus ultimately to the different turbulence models that were used. On the other hand, the overall concentration level in the right stream matches the measurements better in their simulations than in the present ones. Both of these differences may in fact be related. Overall, considering the difference in turbulence modeling which gives rise to different turbulent viscosities and hence different distribution of gas, the agreement between the simulations is as good as may be expected.

To support further model development for the mass transfer, better validation data are still needed, which provide a parametric variation especially of the bubble size that figures as an important parameter in the closure correlations. In this context, the present results show that a precise knowledge of the pressure is required since this has a significant impact on the equilibrium concentrations in gas and liquid. This is an issue that has not received due attention in previous validation experiments. An accompanying measurement of pressure within the test section can serve this purpose and is easily done. To the least a precise specification where exactly the facility is open to the atmosphere must be provided such that the hydrostatic pressure at any point in the system can be calculated. The effect of temperature is relatively small since kinematic viscosity and diffusivity have a similar temperature-dependence which gives only a weak influence on the Schmidt number. A quantification of measurement errors would be very helpful in order to determine which part of eventual deviations should be attributed to the simulation model.

6 ACKNOWLEDEGEMENT

This work has been carried out in the frame of a research project (GZ: RZ 11/3-1) funded by the DFG.

7 NOMENCLATURE

Latin Formula Characters

Symbol	Description	Unit	Symbol	Description	Unit
a_i	interfacial area concentration	m^{-1}	R	universal gas constant	$J\ K^{-1}\ mol^{-1}$
c	molar concentration	$mol\ m^{-3}$	Re	Reynolds number	-
d_B	bubble diameter	m	Sc	Schmidt number	-
D	lateral dimension	m	Sh	Sherwood number	-
D	diffusion coefficient	$m^{-2}\ s^{-1}$	t	time	s

$\boldsymbol{F}$	force per unit volume	N m^{-3}	T	temperature	^{o}C, K
$\boldsymbol{g}$	acceleration of gravity	m s^{-2}	$\mathbf{T}$	stress tensor	N m^{-2}
G	mass flux	kg m^{-2} s^{-1}	$\boldsymbol{u}$	mean velocity	m s^{-1}
H	axial dimension	m	$\boldsymbol{u}'$	fluctuating velocity	m s^{-1}
He	Henry constant	-	W	spanwise dimension	m
J	Superficial velocity = volumetric flux	m s^{-1}	x	lateral coordinate	m
k	mass transfer coefficient	m s^{-1}	X	mole fraction	-
M	molar mass	-	y	axial coordinate	m
p	pressure	Pa	Y	mass fraction	-
r	padial coordinate	m	z	spanwise coordinate	m

Greek Formula Characters

Symbol	Description	Unit	Symbol	Description	Unit
α	phase fraction	-	ν	kinematic viscosity	m^2 s^{-1}
ϵ	turbulent dissipation rate	m^2 s^{-3}	ρ	density, mass concentration	kg m^{-3}
Γ	source term due to mass transfer	kg m^{-3} s^{-1}	σ	surface tension	N m^{-1}
κ	specific turbulent kinetic energy	m^2 s^{-2}	$\boldsymbol{\phi}$	secondary momentum source due to mass transfer	N m^{-3}
μ	dynamic viscosity	kg m^{-1} s^{-1}	ω	turbulent frequency	s^{-1}

Latin Indices

Symbol	Description	Symbol	Description
A	of transferred species	L	liquid phase
eff	effective	mol	molecular
G	gas phase	O_2	of oxygen
H_2O	of water	$turb$	turbulent
$in1$	at inlet 1	X	of any species
$in2$	at inlet 2		

8 REFERENCES

Akgerman, A. and Gainer, J. L., 1972. Predicting gas-liquid diffusivities. *Journal of Chemical and Engineering Data* 17, 372–377.

Ayed, H., Chahed, J., and Roig, V., 2007. Hydrodynamics and mass transfer in a turbulent buoyant bubbly shear layer. *AIChE Journal* 53, 2742–2753.

Battino, R., Rettich, T. R. and Tominaga, T., 1983 The Solubility of Oxygen and Ozone in Liquids. *Journal of Physical and Chemical Reference Data* 12, 163-178.

Brauer, H., 1979. Particle / fluid transport processes. *Progress in Chemical Engineering* 17, 61-99.

Brauer, H., 1981. Mass transfer operations between liquid films and adjoining gas streams. *Progress in Chemical Engineering* 19, 81–111.

Burns, A. D., Frank, T., Hamill, I., Shi, J.-M., 2004. The Favre averaged drag model for turbulence dispersion in Eulerian multi-phase flows. *Proc. 5th Int. Conf. on Multiphase Flow*, ICMF2004, Yokohama, Japan.

Chapman, S. and Cowling, T. G., 1970. The Mathematical Theory of Non-uniform Gases, *Cambridge University Press*.

Clever, H. L., Battino, R., Miyamoto, H., Yampolski, Y. and Young, C. L. , 2014 IUPAC-NIST Solubility Data Series. 103. Oxygen and Ozone in Water, Aqueous Solutions, and Organic Liquids (Supplement to Solubility Data Series Volume 7). *Journal of Physical and Chemical Reference Data* 43, 033102.

Cockx, A., Do-Quang, Z., Audic, J., Line, A. and Roustan, M., 2001. Global and local mass transfer coefficients in waste water treatment process by computational fluid dynamics. *Chemical Engineering and Processing: Process Intensification* 40, 187–194.

Drew, D. A., Passman, S. L., 1998. Theory of Multicomponent Fluids, *Springer*.

Ferrell, R. T. and Himmelblau, D. M., 1967. Diffusion coefficients of nitrogen and oxygen in water. *Journal of Chemical and Engineering Data* 12, 111–115.

Gray, D. E. (Ed.), 1957. American Institute Of Physics Handbook, *McGraw Hill*.

Han, P. and Bartels, D. M., 1996. Temperature dependence of oxygen diffusion in H_2O and D_2O. *Journal of Physical Chemistry* 100, 5597–5602.

Himmelblau, D. M., 1964. Diffusion of dissolved gases in liquids. Chemical Reviews 64, 527–550.

Hlawitschka, M. W., Oßberger, M., Backes, C., Klüfers, P., and Bart, H.-J., 2017a. Reactive mass transfer of single NO bubbles and bubble bouncing in aqueous ferric solutions – A feasibility study. *Oil & Gas Science and Technology* 72, 11.

Hlawitschka, M., Kovats, P., Zähringer, K., and Bart, H.-J. , 2017b. Simulation and experimental validation of reactive bubble column reactors. *Chemical Engineering Science* 170, 306–319.

Hori, Y., Bothe, D., Hayashi, K., Hosokawa, S., and Tomiyama, A., 2020. Mass transfer from single carbon-dioxide bubbles in surfactant-electrolyte mixed aqueous solutions in vertical pipes. *International Journal of Multiphase Flow* 124, 103207.

Hosokawa, S., Tomiyama, A., Misaki, S. and Hamada, T., 2002. Lateral migration of single bubbles due to the presence of wall. *Proc. ASME Joint U.S.-European Fluids Engineering Division Conference,* FEDSM2002*,* Montreal, Canada.

650 Huber, M. L., Perkins, R. A., Laesecke, A., Friend, D. G., Sengers, J. V., Assael, M. J., Metaxa, I.
651 N., Vogel, E., Mares, R. and Miyagawa, K., 2009 New International Formulation for the
652 Viscosity of H_2O. *Journal of Physical and Chemical Reference Data* 38, 101–125.

653 Ishii, M. and Hibiki, T., 2011. Thermo-fluid dynamics of two-phase flow. *Springer*, 2nd ed.

654 Ishii, M. and Zuber, N., 1979. Drag coefficient and relative velocity in bubbly, droplet or
655 particulate flows. *AIChE Journal* 25, 843–855.

656 Kell, G. S., 1975. Density, thermal expansivity, and compressibility of liquid water from 0° to
657 150°C: Correlations and tables for atmospheric pressure and saturation reviewed and
658 expressed on 1968 temperature scale. *Journal of Chemical and Engineering Data* 20, 97–105.

659 Kipping, R., Kryk, H., and Hampel, U., 2020. Experimental analysis of gas phase dynamics in a
660 lab scale bubble column operated with deionized water and NaOH solution under uniform
661 bubbly flow conditions. *Chemical Engineering Science* 229, 116056.

662 Kovats, P., Thevenin, D., and Zaehringer, K., 2018. Characterizing fluid dynamics in a bubble
663 column aimed for the determination of reactive mass transfer. *Heat and Mass Transfer* 54,
664 453–461.

665 Krauß, M. and Rzehak, R., 2017. Reactive absorption of CO2 in NaOH: Detailed study of
666 enhancement-factor models. *Chemical Engineering Science* 166, 193–209.

667 Krauß, M. and Rzehak, R., 2018. Reactive absorption of CO2 in NaOH: An Euler-Euler
668 simulation study. *Chemical Engineering Science* 181, 199–214.

669 Liao, J., Ziegenhein, T., and Rzehak, R., 2016. Bubbly flow in an airlift column: a CFD study.
670 *Journal of Chemical Technology & Biotechnology* 91, 2904–2915.

671 Menter, F. R., 2009. Review of the shear-stress transport turbulence model experience from
672 an industrial perspective. *International Journal of Computational Fluid Dynamics* 23, 305–316.

673 Merker, D., Böhm, L., Oßberger, M., Klüfers, P., and Kraume, M., 2017. Mass Transfer in
674 Reactive Bubbly Flows – A Single-Bubble Study. *Chemical Engineering Technology* 40 1391–
675 1399.

676 Mewes, D. and Wiemann, D., 2003. Two-phase flow with mass transfer in bubble columns.
677 *Chemical Engineering Technology* 26, 862–868.

678 Parekh, J. and Rzehak, R., 2018. Euler-Euler multiphase CFD-simulation with full Reynolds
679 stress model and anisotropic bubble-induced turbulence. *International Journal of Multiphase*
680 *Flow* 99, 231–245.

681 Rettich, T. R., Battino, R. and Wilhelm, E., 2000. Solubility of gases in liquids. 22. High-precision
682 determination of Henry's law constants of oxygen in liquid water from T=274 K to T=328 K.
683 *Journal of Chemical Thermodynamics* 32, 1145–1156.

684 Roig, V. and Larue de Tournemine, A., 2007. Measurement of interstitial velocity of
685 homogeneous bubbly flows at low to moderate void fraction. *Journal of Fluid Mechanics* 572,
686 87–110.

687 Rzehak, R. and Krepper, E., 2013. Bubble-induced turbulence: Comparison of CFD models.
688 *Nuclear Engineering and Design* 258, 57–65.

689 Rzehak, R. and Krepper, E., 2013a. CFD modeling of bubble-induced turbulence. *International*
690 *Journal of Multiphase Flow* 55, 138–155.

691 Rzehak, R. and Krepper, E., 2015. Bubbly flows with fixed polydispersity: Validation of a
692 baseline closure model. *Nuclear Engineering and Design* 287, 108–118.

693 Rzehak, R. and Kriebitzsch, S., 2015. Multiphase CFD-simulation of bubbly pipe flow: A code
694 comparison. *International Journal of Multiphase Flow* 68, 135–152.

695 Rzehak, R., Krepper, E., Liao, Y., Ziegenhein, T., Kriebitzsch, S. and Lucas, D., 2015. Baseline
696 model for the simulation of bubbly flows. *Chemical Engineering and Technology* 38, 1972–
697 1978.

698 Rzehak, R., Krepper, E., 2016. Euler-Euler simulation of mass-transfer in bubbly flows.
699 *Chemical Engineering Science* 155, 459–568.

700 Rzehak, R. 2016. Modeling of mass-transfer in bubbly flows encompassing different
701 mechanisms. *Chemical Engineering Science* 151, 139–143.

702 Rzehak, R., Ziegenhein, T., Kriebitzsch, S., Krepper, E., and Lucas, D., 2017.
703 Unified modeling of bubbly flows in pipes, bubble columns, and airlift columns.
704 *Chemical Engineeing Science* 157, 147–158.

705 Rzehak, R., Krauß, M., Kovats, P., and Zähringer, K., 2017a. Fluid dynamics in a bubble column:
706 New experiments and simulations. *International Journal of Multiphase Flow* 89, 299–312.

707 Sander, R., 2015. Compilation of Henry's law constants (version 4.0) for water as solvent.
708 Atmospheric Chemistry and Physics 15, 4399–4981.

709 Shi, P. and Rzehak, R., 2018. Bubbly flow in stirred tanks: Euler-Euler / RANS modeling.
710 *Chemical Engineering Science* 190, 419–435.

711 Solsvik, J., 2018. Lagrangian modeling of mass transfer from a single bubble rising in stagnant
712 liquid. *Chemical Engineering Science* 190, 370–383.

713 Taborda, M. A. and Sommerfeld, M., 2021. Reactive LES-Euler/Lagrange modelling of bubble
714 columns considering effects of bubble dynamics. *Chemical Engineering Journal* 407, 127222.

715 Tomiyama, A., Kataoka, I., Zun, I., and Sakaguchi, T., 1998. Drag coefficients of single bubbles
716 under normal and micro gravity conditions. *JSME International Journal B* 41, 472–479.

717 Tomiyama, A., Tamai, H., Zun, I., and Hosokawa, S., 2002. Transverse migration of single
718 bubbles in simple shear flows. *Chemical Engineering Science* 57, 1849–1858.

719 Vargaftik, N. B., Volkov, B. N. and Voljak, L. D., 1983. International tables of the surface tension
720 of water. *Journal of Physical and Chemical Reference Data* 12, 817–820.

721 Verhallen, P., Oomen, L., Elsen, A., Kruger, J. and Fortuin, J., 1984. The diffusion coefficients
722 of helium, hydrogen, oxygen and nitrogen in water determined from the permeability of a
723 stagnant liquid layer in the quasi-steady state. *Chemical Engineering Science* 39, 1535–1541.

724 Wagner, W. and Pruss, A., 2002. The IAPWS formulation 1995 for the thermodynamic
725 properties of ordinary water substance for general and scientific use. *Journal of Physical and*
726 *Chemical Reference Data* 31, 387–535.

727 Wise, D. and Houghton, G. 1966. The diffusion coefficients of ten slightly soluble gases in
728 water at 10-60°C. *Chemical Engineering Science* 21, 999–1010.

729 Yeoh, G. H. and Tu, J. Y., 2010. Computational Techniques for Multiphase Flows — Basics and
730 Applications, *Butterworth-Heinemann*.

731 Zhang, C., Yuan, X., Luo, Y., and Yu, G., 2018. Prediction of species concentration distribution
732 using a rigorous turbulent mass diffusivity model for bubble column reactor simulation part I:
733 Application to chemisorption process of CO2 into NaOH solution. *Chemical Engineering*
734 *Science* 184, 161–171.

735 Zidouni, F., Krepper, E., Rzehak, R., Rabha, S., Schubert, M., Hampel, U., 2015. Simulation of
736 gas-liquid flow in a helical static mixer. *Chemical Engineering Science* 137, 476-486.

737 Ziegenhein, T., Rzehak, R., Krepper, E. and Lucas, D., 2013. Numerical simulation of
738 polydispersed flow in bubble-columns with the inhomogeneous multi-size-group model.
739 *Chemie Ingenieur Technik* 85, 1080–1091.

740 Ziegenhein, T., Rzehak, R., Lucas, D., 2015. Transient simulation for large scale flow in bubble
741 columns. *Chemical Engineering Science* 122, 1-13.

742 Ziegenhein, T., Rzehak, R., Ma, T., and Lucas, D., 2017. A unified approach for modeling
743 uniform and non-uniform bubbly flows. *Canadian Journal of Chemical Engineering* 95, 170–
744 179.